Irreversibility in bacterial turbulence: Insights from the mean-bacterial-velocity model

Kolluru Venkata Kiran,[1,*] Anupam Gupta,[2,†] Akhilesh Kumar Verma,[3,‡] and Rahul Pandit[1,§]

[1]*Centre for Condensed Matter Theory, Department of Physics, Indian Institute of Science, Bangalore 560012, India*

[2]*Department of Physics, Indian Institute of Technology (IIT) Hyderabad, Kandi, Sangareddy, Telangana 502285, India*

[3]*Mathematics Institute, Zeeman Building, University of Warwick, Coventry CV4 7AL, United Kingdom*

(Received 2 February 2022; accepted 25 January 2023; published 22 February 2023)

We use the mean-bacterial-velocity model to investigate the irreversibility of two-dimensional (2D) bacterial turbulence and to compare it with its 2D fluid-turbulence counterpart. We carry out extensive direct numerical simulations of Lagrangian tracer particles that are advected by the velocity field in this model. We demonstrate how the statistical properties of these particles help us to uncover an important, qualitative way in which irreversibility in bacterial turbulence is different from its fluid-turbulence counterpart: For large but negative (or large and positive) values of the activity (or friction) parameter, the probability distribution functions of energy increments, along tracer trajectories, or the power are positively skewed; so irreversibility in bacterial turbulence can lead, on average, to particles gaining energy faster than they lose it, which is the exact opposite of what is observed for tracers in 2D fluid turbulence.

DOI: 10.1103/PhysRevFluids.8.023102

I. INTRODUCTION

Active-matter systems are fundamentally time irreversible; their constituents consume energy from the environment and convert it to systematic motion [1–4]. Dense bacterial suspensions, which are important examples of active systems, show spatiotemporal evolution that is reminiscent of flows in turbulent fluids [5–8]. We present a quantification of the inherent irreversibility of such bacterial turbulence by following the dynamics of Lagrangian tracer particles, as in classical fluid turbulence. Most classical fluid flows are turbulent; they can attain a nonequilibrium, but statistically steady, state (NESS), if the energy injection into the fluid, say, by an external force, is balanced by viscous dissipation. Far away from boundaries, this NESS is statistically homogeneous and isotropic if we consider length scales that are much smaller than the energy-injection scale l_f [9,10]. Two important characteristics of this NESS are (a) the distribution of energy over a large range of length scales and (b) the temporal irreversibility of turbulent flows. This irreversibility is not easily apparent if we look at movies, played forward or backward in time, of Lagrangian particles, or *tracers*, that are advected by turbulent flows; however, the statistics of such tracers or inertial particles in turbulent flows yields signatures of this irreversibility [11–19] if we analyze (a) the increments

$$W(t,\tau) \equiv E(t+\tau) - E(t) \tag{1}$$

*kollurukiran@iisc.ac.in
†agupta@phy.iith.ac.in
‡akvermajnusps@gmail.com
§rahul@iisc.ac.in

of the particle energy E at time t or (b) the power

$$p_L(t) \equiv \frac{dE}{dt} = a_L v_L, \tag{2}$$

with v_L being the magnitude of the tracer velocity and a_L being the component of its acceleration along its trajectory. It has been found that probability distribution functions (PDFs) of W and p_L, obtained by averaging over t and the trajectories of all tracers, are negatively skewed [11,16,18,20–23]; i.e., on average, such tracers lose energy faster than they gain it. We show how to use these PDFs to bring out differences between irreversibility in fluid turbulence and its counterpart in *bacterial turbulence* [7,24–30], an exciting new form of spatiotemporal chaos in active fluids. We carry out an extensive study of the irreversibility of bacterial turbulence in the mean-bacterial-velocity model [7]. Our work uncovers an important, qualitative way in which irreversibility in bacterial turbulence is different from that in fluid turbulence: For large but negative (or large and positive) values of the *activity* (or *friction*) parameter α (see below), the PDFs of $W(\tau)$ or p_L are *positively* skewed; this implies that irreversibility in bacterial turbulence can lead, on average, to *particles gaining energy faster than they lose it*, for certain ranges of values of α.

II. THE MODEL

Hydrodynamic models have been developed to describe turbulence in dense, quasi-two-dimensional (quasi-2D) bacterial suspensions [7,8,24–29,31–35]. We use the mean-bacterial-velocity model [7] or the Toner-Tu-Swift-Hohenberg (TTSH) model [8,36], for the incompressible velocity field $\boldsymbol{u}(\mathbf{x}, t)$; this model has been employed to study turbulence in dense suspensions of *Bacillus subtilis*:

$$\frac{\partial \boldsymbol{u}}{\partial t} + \lambda_0 \boldsymbol{u} \cdot \boldsymbol{\nabla} \boldsymbol{u} = -\boldsymbol{\nabla} P - (\alpha + \beta |u|^2)\boldsymbol{u} + \Gamma_0 \nabla^2 \boldsymbol{u} - \Gamma_2 \nabla^4 \boldsymbol{u},$$
$$\boldsymbol{\nabla} \cdot \boldsymbol{u} = 0. \tag{3}$$

Here, $P(\mathbf{x}, t)$ is the pressure at point $\mathbf{x}$ and time t; the constant density ρ is set to unity [37]. We use periodic boundary conditions in all directions because we concentrate on statistically homogeneous and isotropic bacterial turbulence. We restrict ourselves to two dimensions as most experiments in this field have been conducted in quasi-2D systems. The parameters $\Gamma_0 < 0$ and $\Gamma_2 < 0$; a spatial Fourier transform of Eq. (3), followed by a linear-stability analysis about the spatially uniform state, yields the wave vectors $\mathbf{k}$, with magnitude k, for which there are linearly unstable modes. We define the following characteristic length, velocity, and time scales, respectively:

$$\Lambda = 2\pi \sqrt{\frac{2\Gamma_2}{\Gamma_0}}, \quad v_0 = \sqrt{\frac{|\Gamma_0|^3}{\Gamma_2}}, \quad \theta = \frac{\Lambda}{v_0}. \tag{4}$$

These unstable modes provide a source of energy injection into the system [38]; this energy is dissipated by (a) the linearly stable modes, (b) the cubic term with the coefficient $\beta > 0$, and (c) the linear term with the coefficient α, if $\alpha > 0$. Moreover, there is energy injection, or *activity*, if $\alpha < 0$; and $\Gamma_0 < 0$ and $\lambda_0 \neq 1$ also induce activity [36] ($\lambda_0 > 1$ for *pusher swimmers* such as *B. subtilis* (see, e.g., Refs. [7,24,39])). The interplay between these energy-injection and dissipation terms leads to a NESS with self-sustained, turbulence-type patterns [30]. The effective viscosity

$$k^2 \nu_{\text{eff}}(k) = \left(\alpha + 2\beta u_{\text{rms}}^2 + \Gamma_0 k^2 + \Gamma_2 k^4\right) \tag{5}$$

can be used to rewrite Eq. (3) in a Navier-Stokes form (see the Appendix and Ref. [30]). Clearly, the wave numbers k at which energy is injected (dissipated) are those with $\nu_{\text{eff}}(k) < 0$ [$\nu_{\text{eff}}(k) > 0$]; the root-mean-square velocity u_{rms} must be obtained from a calculation (see below). We can tune different parameters in Eq. (5) to vary $\nu_{\text{eff}}(k)$; for example, run D (see Table I) is an illustrative one in which energy is injected predominantly at one wave number. We solve Eq. (3) by a pseudospectral

TABLE I. Parameters for our DNSs. For all the runs listed in the table, $\Gamma_0 = -0.045$, $\beta = 0.5$, and $\lambda_0 = 3.5$.

Run	Γ_2	α	δt	Λ	θ	v_0
A1–A12	9×10^{-5}	[a]	2×10^{-4}	0.40	0.40	1.0
B	9×10^{-5}	-4	1×10^{-5}	0.40	0.40	1.0
C	9×10^{-5}	1	5×10^{-5}	0.40	0.40	1.0
D	3.6×10^{-5}	14	1×10^{-4}	0.25	0.16	1.60

[a]Runs A1–A12 use $\alpha = -4, -3.5, -2.5, -1.5, -1, -0.5, 0, 1, 3, 3.5, 4$, and 5, respectively.

direct numerical simulation (DNS) [40,41] with $N^2 = 1024^2$ collocation points and the parameters in Table I. We employ the second-order integrating-factor method IFRK2 for time marching [42]; we have checked in representative cases that our results are unchanged if we use $N^2 = 2048^2$ collocation points. We hold λ_0, β, and Γ_0 fixed, and we tune the activity principally by varying α. We follow Refs. [7,43] in restricting our model parameters to experimentally realizable regimes. The average velocities observed in experiments on *B. subtilis* are $\simeq 25$ μm/s, at normal oxygen concentrations, and the typical viewing area is 400×400 μm; we map these to the constant velocity scale v_0 and the simulation box area $L \times L$, respectively. This gives us the scale factors of $25/v_0$ and $4 \times 10^{-2}/L$ for mapping velocities and lengths, respectively, in our DNSs to their experimental counterparts.

III. RESULTS

In Figs. 1(a)–1(c), we present filled contour plots of the vorticity $\boldsymbol{\omega}(\mathbf{x}, t) = \boldsymbol{\nabla} \times \boldsymbol{u}(\mathbf{x}, t)$, with some tracers shown via black points, for the representative runs A1, A8, and D, respectively (see Table I). In Figs. 1(d)–1(i), we give log-log plots versus $k\Lambda$ of the k-shell-averaged energy spectrum $\mathcal{E}(k)$ and energy flux $\Pi(k)$:

$$\mathcal{E}(k) = \frac{1}{2} \sum_{k'=k-1/2}^{k'=k+1/2} \langle \widetilde{\boldsymbol{u}}(\mathbf{k}') \cdot \widetilde{\boldsymbol{u}}(-\mathbf{k}') \rangle_t,$$

$$\Pi(k) = -\lambda_0 \sum_{k'=0}^{k'=k} \sum_{k''=k'-1/2}^{k''=k'+1/2} [\langle \widetilde{\boldsymbol{u}}(-\mathbf{k}'') \cdot \mathbf{P}(\mathbf{k}'') \cdot \widetilde{(\boldsymbol{u} \cdot \boldsymbol{\nabla} \boldsymbol{u})}(\mathbf{k}'') \rangle_t]. \tag{6}$$

Here, tildes denote spatial Fourier transforms, $\langle \cdot \rangle_t$ is the time average over the NESS, and the transverse projector $\mathbf{P}(\mathbf{k})$ has the components $P_{ij}(\mathbf{k}) = \delta_{ij} - \frac{k_i k_j}{k^2}$. The total fluid energy, root-mean-square velocity, integral length scale, integral time scale, and integral-scale Reynolds number are

$$\mathcal{E}_T = \sum_k \mathcal{E}(k), \quad u_{\rm rms} = \sqrt{2\mathcal{E}_T}, \quad L_I = \frac{\sum_k [\mathcal{E}(k)/k]}{\sum_k \mathcal{E}(k)},$$

$$T_I = L_I / u_{\rm rms}, \quad {\rm Re}_{L_I} \equiv u_{\rm rms} L_I^3 / \Gamma_2, \tag{7}$$

respectively. The gray-shaded areas in Figs. 1(d)–1(i) indicate the ranges of k for which $\nu_{\rm eff}(k) < 0$. For the runs in Table I, there is no range of k over which $\Pi(k)$ remains constant, unlike its fluid-turbulence counterpart; so we cannot identify inverse- or forward-cascade regimes in $\mathcal{E}(k)$. However, $\mathcal{E}(k)$ is spread over a large range of k, and the temporal evolution of $\boldsymbol{u}$ is chaotic, so the bacterial-turbulence NESS for this model [Eq. (3)] displays spatiotemporal chaos. In Figs. 2(a)–2(d) we present plots versus α of $u_{\rm rms}/v_0$, L_I/Λ, T_I/θ, and ${\rm Re}_{L_I}$, respectively (runs A1–A12); as α moves from the *activity regime* ($\alpha < 0$) to the *frictional regime* ($\alpha > 0$), $u_{\rm rms}/v_0$, L_I/Λ, and ${\rm Re}_{L_I}$ decrease, but T_I/θ first decreases and then increases because $u_{\rm rms}$ decreases more rapidly than L_I.

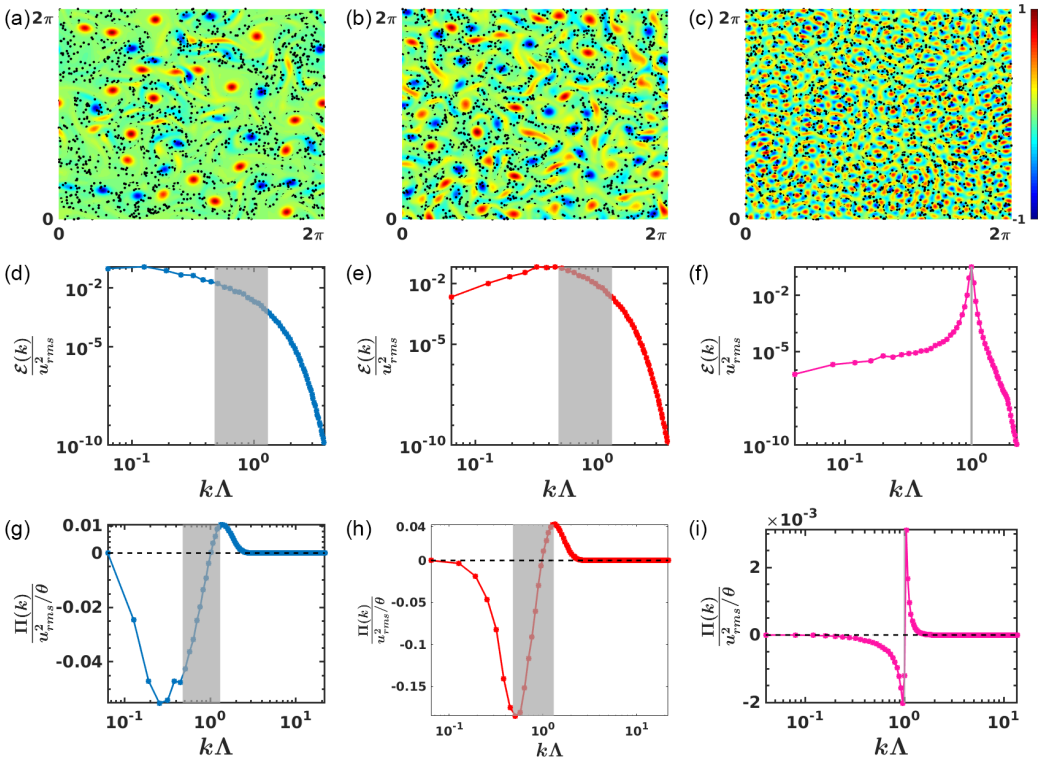

FIG. 1. Plots for runs A1, A8, and D (Table I): (a)–(c) Filled contour plots of the vorticity $\boldsymbol{\omega}(\mathbf{x}, t)$, with some tracers (black points), at a representative time in the NESS; log-log (base 10) plots vs $k\Lambda$ of (d)–(f) the energy spectrum $\mathcal{E}(k)$ and (g)–(i) the energy flux $\Pi(k)$ [Eq. (6)]; the gray-shaded areas indicate the ranges of k for which $\nu_{\text{eff}}(k) < 0$ [Eq. (5)].

The velocity $\mathbf{v}_L(t)$ of a tracer at $\mathbf{x}_L(t)$ is

$$\frac{d\mathbf{x}_L(t)}{dt} \equiv \mathbf{v}_L(t) = \boldsymbol{u}(\mathbf{x}_L(t), t). \tag{8}$$

We track $N_p = 10\,000$ tracers, employ the second-order Runge-Kutta method for time marching, and evaluate $\boldsymbol{u}(\mathbf{x}_L(t), t)$ at off-grid points via bilinear interpolation [44–46]; to get good statistics, we use very long runs (3×10^6 time steps per particle). The acceleration of a tracer particle is

$$\begin{aligned}\mathbf{a}(\mathbf{x}_L, t) &\equiv \frac{\partial \boldsymbol{u}}{\partial t} + (\boldsymbol{u}\cdot\boldsymbol{\nabla})\boldsymbol{u}|_{x_L(t)} \\ &= -\boldsymbol{\nabla} P_{\text{eff}} - (1-\lambda_0)(\boldsymbol{u}\times\boldsymbol{\omega}) - (\alpha + \beta|u|^2)\boldsymbol{u} + \Gamma_0\nabla^2\boldsymbol{u} - \Gamma_2\nabla^4\boldsymbol{u}|_{x_L(t)},\end{aligned} \tag{9}$$

where the effective pressure $P_{\text{eff}} = P - \frac{1}{2}(1-\lambda_0)\boldsymbol{u}\cdot\boldsymbol{u}$; the component of this acceleration along the tracer's trajectory yields a_L, whence we get p_L [Eq. (2)] and its normalized PDF $\mathcal{P}(\frac{p_L}{\langle p_L^2\rangle^{1/2}})$. From the time series of particle energies (Fig. 4) we obtain the energy-increment PDFs $\mathcal{P}(\frac{W(\tau)}{\langle W^2(\tau)\rangle^{1/2}})$, for various values of $\tau < T_l$. Both these PDFs have zero mean [Figs. 3(a) and 3(b)], because we are considering a statistically steady state in which the mean energy input is balanced by dissipation, but they are asymmetrical; we characterize this asymmetry by computing the skewnesses

$$\mathcal{P}_{\text{Sk}} = \frac{\langle p_L^3\rangle}{\langle p_L^2\rangle^{\frac{3}{2}}} \quad \text{and} \quad \mathcal{W}_{\text{Sk}}(\tau) = \frac{\langle W^3(\tau)\rangle}{\langle W^2(\tau)\rangle^{\frac{3}{2}}}, \tag{10}$$

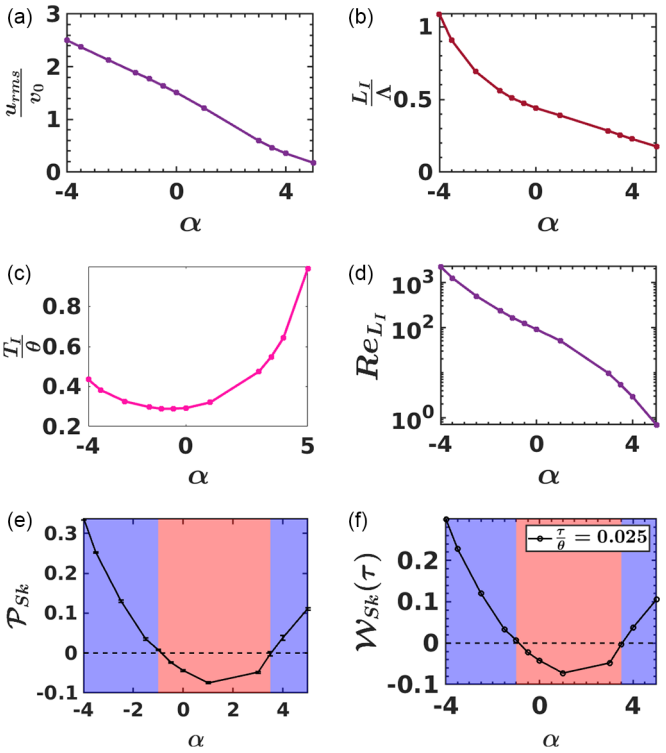

FIG. 2. Plots vs α of (a) $u_{\rm rms}/v_0$, (b) L_I/Λ, (c) T_I/θ, (d) Re_{L_I}, (e) the skewness $\mathcal{P}_{\rm Sk}$, and (f) $\mathcal{W}_{\rm Sk}(\tau)$ for $\tau/\theta = 0.025$; in (e) and (f), blue and pink shading indicate ranges of α in which the skewnesses are positive and negative, respectively.

which we plot versus α in Figs. 2(e) and 2(f), respectively. We observe that $\mathcal{P}_{\rm Sk} > 0$ in the large-activity, $\alpha < -2$, and extreme-friction, $\alpha > 3.5$, regions (shaded blue). This is in *stark contrast* to 2D fluid turbulence [11], where $\mathcal{P}_{\rm Sk} < 0$. The values of α for which $\mathcal{P}_{\rm Sk} < 0$ lead to NESSs that are characterized by *flight-crash* events in which, on average, $E(t)$ builds up slowly but decays rapidly. (In 2D Faraday-wave experiments, $\mathcal{P}_{\rm Sk} > 0$ has been attributed to the temporal coherence of these waves and has been removed by filtering [47].) For runs B and D we also find $\mathcal{P}_{\rm Sk} > 0$. Runs B and

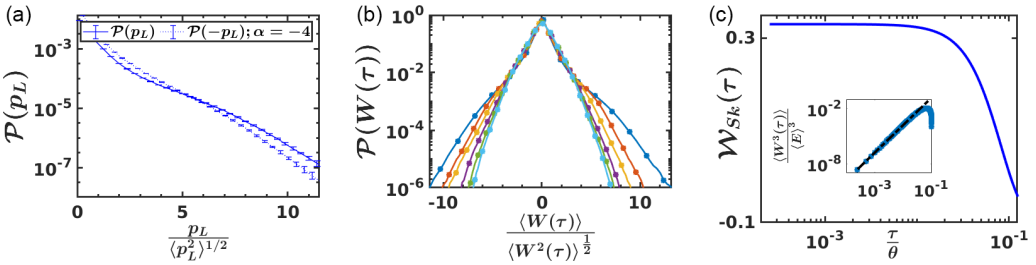

FIG. 3. Plots for run B: Semilog plot of the normalized PDFs (a) $\mathcal{P}(p_L)$ and (b) $\mathcal{P}(W(\tau))$, with τ/θ going from 0.025 to 0.08 to 0.13 to 0.25 to 0.38 to 0.50, as we move from the outermost to the innermost curve; in (a), negative values of p_L (dashed curve) are reflected about the vertical axis to highlight the asymmetry of $\mathcal{P}(p_L)$. (c) Log-log (base 10) plot vs τ/θ of the skewness $\mathcal{W}_{\rm Sk}(\tau)$. Inset: for the same range of τ/θ, a log-log plot vs τ/θ of $\langle W^3(\tau)\rangle/\langle E\rangle^3$; the dashed black line is a fit to $\langle W^3(\tau)\rangle/\langle E\rangle^3 \sim (\tau/\theta)^3$.

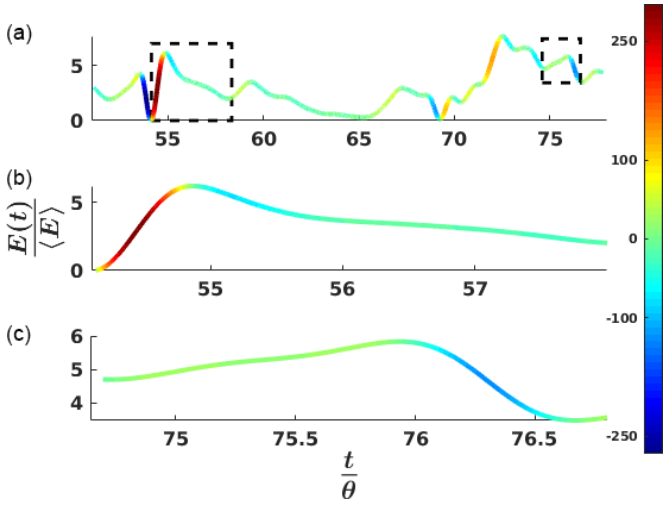

FIG. 4. (a)–(c) Plots of the normalized energy $E(t)/\langle E\rangle$ vs the normalized time t/θ along a representative particle trajectory from run A1; the colors along the trajectory indicate the value of p_L.

C, which are similar to runs A1 and A8, respectively, but with smaller time steps δt, illustrate that the sign of $\mathcal{P}_{\rm Sk}$ is robust and does not change with δt. We find $\mathcal{P}_{\rm Sk} > 0$ in other parameter regimes too (see the illustrative simulations outlined in Table I of the Supplemental Material [48]); so the positive skewness, for the active turbulence in the high-activity regime, is a robust result.

In Fig. 4(a) we plot the time series of $E/\langle E\rangle$ of a typical particle. We also show magnified regions of this time series to exhibit a flight-crash event [Fig. 4(c)], of the type that is predominant in fluid turbulence, and an event in which $E(t)$ builds up faster than it decays [Fig. 4(b)]. In the large-activity and extreme-friction regions mentioned above, the predominance of events such as the one shown in Fig. 4(b) leads to $\mathcal{P}_{\rm Sk} > 0$ and, for small τ/θ, $\mathcal{W}_{\rm Sk}(\tau) = \frac{\langle W^3(\tau)\rangle}{\langle W^2(\tau)\rangle^{\frac{3}{2}}} > 0$, because $\lim_{\tau\to 0} W(\tau, t) \sim p_L(t)$. Furthermore, for $\tau/\theta \ll 1$, we obtain the Taylor-expansion result $\langle W^3(\tau)\rangle \sim \tau^3$, for which we give a representative plot in the inset of Fig. 3(c). As τ decreases, the tails of $\mathcal{P}(\frac{W(\tau)}{\langle W^2(\tau)\rangle^{1/2}})$ widen, as in fluid turbulence [11,49].

We find that that fast-gain and slow-loss events [Fig. 4(b)] occur on the particle-acceleration time scale τ_a, which we obtain from the first zero crossing of the normalized acceleration autocorrelation function. Therefore, if we average $p_L(t)$ over times $O(\tau_a)$, we obtain $\mathcal{P}_{\rm Sk} < 0$ (see the Supplemental Material for details).

The sign of $\mathcal{P}_{\rm Sk}$ [and, for small τ/θ, the sign of $\mathcal{W}_{\rm Sk}(\tau)$] displays the following correlation with the scale-by-scale energy budget in Fourier space, where we can identify the k dependence of the energy contributions from the terms with coefficients α, Γ_0, and λ_0 in Eq. (3). The contributions of the first two terms dominate over those of the third term when $\mathcal{P}_{\rm Sk} > 0$, as we show in detail in the Appendix. In 2D incompressible flows, the Okubo-Weiss parameter [40,50–52] distinguishes between vortical and strain-dominated regions. We define this, along particle trajectories, as follows:

$$Q_L(t) = \left.\frac{\omega^2 - \sigma^2}{4}\right|_{x_L(t)}, \tag{11}$$

where $\omega^2 = \frac{1}{2}\sum_{i,j}(\partial_i u_j - \partial_j u_i)^2$ and $\sigma^2 = \frac{1}{2}\sum_{i,j}(\partial_i u_j + \partial_j u_i)^2$, with $i, j = 1, 2$. $Q_L > 0$ ($\equiv Q_L^+$), in vortical regions, and $Q_L < 0$ ($\equiv Q_L^-$), in strain-dominated regions. The PDF $\mathcal{P}(\frac{Q_L}{\langle Q_L^2\rangle^{1/2}})$ is positively skewed; its skewness $\mathcal{Q}_{\rm Sk}$ decreases with increasing α but remains positive throughout the range of α for runs A1–A12 [inset of Fig. 5(a)]. For high activities, the cumulative PDF $\mathcal{C}(Q_L^+)$,

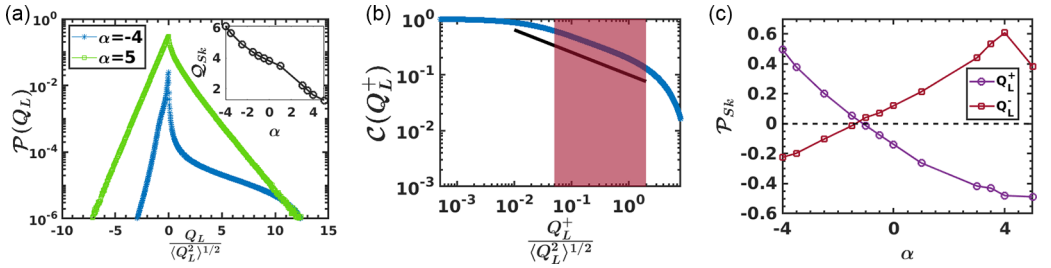

FIG. 5. (a) Semilog plots of $\mathcal{P}(Q_L)$ for runs A1 (blue) and A13 (green). The inset gives the plot vs α of skewness, $\mathcal{Q}_{\rm Sk}$, for $\mathcal{P}(Q_L)$. (b) Log-log plot of $\mathcal{C}(Q_L^+)$ for run A1; the shaded region shows a power law, and the solid black line gives the fit $\mathcal{C}(Q_L^+) \sim [Q_L^+]^{-\vartheta}$, with $\vartheta = 0.37 \pm 0.04$. (c) Plots vs α of $\mathcal{P}_{\rm Sk}$ for the conditioned PDFs (see text) $\mathcal{P}(p_L|Q_L^+)$ (violet) and $\mathcal{P}(p_L|Q_L^-)$ (maroon).

shows a power-law tail for Q_L^+ [Fig. 5(b)], a unique feature of the bacterial-turbulence model we study [53]; in contrast, for the high-friction regime ($\alpha > 2$), the tail of $\mathcal{P}(Q_L)$ has a faster-than-exponential decay, for small and positive values of Q_L, as in 2D fluid turbulence. Furthermore, in the large-activity regime $\alpha \leqslant -2$, the positivity of $\mathcal{P}_{\rm Sk}$ arises from vortical regions, whereas, in the high-friction regime $\alpha \geqslant 2$, this positive skewness comes from the strain-dominated regions, which we surmise from Fig. 5(c), where we plot $\mathcal{P}_{\rm Sk}$ for the conditioned PDFs $\mathcal{P}(p_L|Q_L^+)$ and $\mathcal{P}(p_L|Q_L^-)$. This is an important insight.

IV. DISCUSSION

We have shown that, in 2D bacterial turbulence in the mean-bacterial-velocity model, the positivity of these skewnesses occurs because of the activity, which we tune via the parameter α. If the spectral energy transfer, because of the advective nonlinearity, is dominant or is comparable to the spectral energy contributions from other active terms, the signs of these skewnesses are the same as in 3D and 2D Navier-Stokes turbulence; otherwise, they are positive (see Fig. 1). This indicates the presence of an energy-transfer mechanism that is different from 3D Navier-Stokes turbulence but similar to the one discussed in the context of active-nematic turbulence [54].

Quasi-2D experiments on dense suspensions of aerobic bacteria, e.g., *B. subtilis*, show that the average speed of bacterial flow increases with the oxygen concentration [5,6,55]. We can increase the activity by making α large and negative. In experiments, the activity can be increased by enhancing the oxygen concentration, because the polar-ordered velocity scale $v_p = \sqrt{\frac{|\alpha|}{\beta}}$ is a measure of the swimming speed of bacteria. $u_{\rm rms} \propto \alpha$ (cf. Ref. [43]), and in the frictional or $\alpha > 0$ regime, the value of α can be tuned in experiments by changing the bottom friction or the air-drag-induced friction (see Supplemental Material [48] for details). Therefore experiments on dense bacterial suspensions should be able to examine irreversibility in bacterial turbulence as a function of the activity as we have done in Fig. 2. It is important to use the methods we describe here to explore irreversibility of bacterial turbulence in other models [27,31,32] and also in models for active fluids [56,57] and active nematics [33,34,54]. We propose to carry out such studies in the near future.

ACKNOWLEDGMENTS

We thank J. K. Alageshan, V. Deshpande (NVIDIA), N. B. Padhan, S. Shukla, and S. S. V. Kolluru for discussions; CSIR, the National Supercomputing Mission (NSM), and SERB (India) for support; and SERC (IISc) for computational resources. A.G. is thankful for computational and financial support from DST-India NSM R&D-HPC Application No. 2021/05 and Seed Grant No. IITH/2020/09.

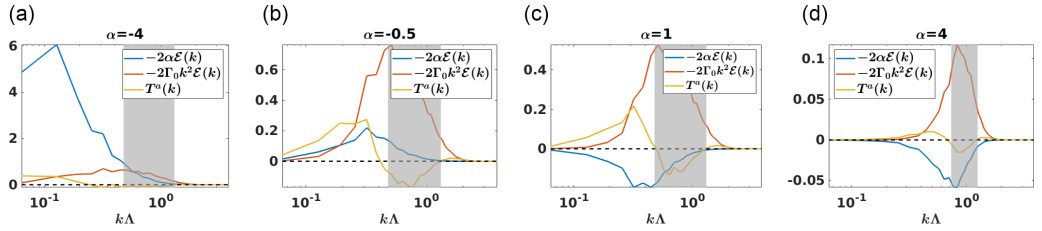

FIG. 6. Semilog plots vs $k\Lambda$ of $T^a(k)$ (yellow), $-2\alpha\mathcal{E}(k)$ (blue), and $-2\Gamma_0 k^2\mathcal{E}(k)$ (orange); the gray-shaded areas indicate the ranges of k for which $\nu_{\rm eff}(k) < 0$ for (a) run A1, (b) run A7, (c) run A8, and (d) run A11.

APPENDIX: ENERGY BUDGET

For the shell-averaged energy spectrum

$$\mathcal{E}(k) = \frac{1}{2}\sum_{k'=k-1/2}^{k'=k+1/2} \langle \widetilde{\boldsymbol{u}}(\mathbf{k}')\cdot\widetilde{\boldsymbol{u}}(-\mathbf{k}')\rangle_t$$

we have [30]

$$\partial_t \mathcal{E}(k) = T^a(k) - T^c(k) - 2\alpha\mathcal{E}(k) - 2\Gamma_0 k^2\mathcal{E}(k) - 2\Gamma_2 k^4\mathcal{E}(k), \tag{A1}$$

where $T^a(k)$ and $T^c(k)$, the k-shell averaged contributions from the advective and cubic terms in Eq. (3), respectively, are

$$T^a(k) = -\lambda_0 \sum_{k'=k-1/2}^{k'=k+1/2} \langle \widetilde{\boldsymbol{u}}(-\mathbf{k}')\cdot\mathbf{P}(\mathbf{k}')\cdot\widetilde{(\boldsymbol{u}\cdot\nabla\boldsymbol{u})}(\mathbf{k}')\rangle_t,$$

$$T^c(k) = \beta \sum_{k'=k-1/2}^{k'=k+1/2} \langle \widetilde{\boldsymbol{u}}(-\mathbf{k}')\cdot\mathbf{P}(\mathbf{k}')\widetilde{(|\boldsymbol{u}|^2\boldsymbol{u})}(\mathbf{k}')\rangle_t, \tag{A2}$$

with $P_{ij}(\mathbf{k}) = \delta_{ij} - \frac{k_i k_j}{k^2}$ being the transverse projector and $\langle\cdot\rangle_t$ being the average over time t. The flux of energy arising from the advective term is

$$\Pi(k) = -\sum_{k'=0}^{k'=k} T^a(k'). \tag{A3}$$

The effective viscosity

$$k^2\nu_{\rm eff}(k) = \left(\alpha + 2\beta u_{\rm rms}^2 + \Gamma_0 k^2 + \Gamma_2 k^4\right)$$

can be used to rewrite Eq. (3), in a form that resembles the Navier-Stokes equation, with the constant viscosity ν replaced by $\nu_{\rm eff}(k)$. To obtain Eq. (5), we use the approximation $T^c(k) \simeq -4\beta u_{\rm rms}^2\mathcal{E}(k)$ suggested in Ref. [30]; here, $u_{\rm rms}$ must be obtained from our calculation. Clearly, the wave numbers k at which energy is injected (dissipated) are those with $\nu_{\rm eff}(k) < 0$ [$\nu_{\rm eff}(k) > 0$].

The sign of $\mathcal{P}_{\rm Sk}$ [and, for small τ/θ, the sign of $\mathcal{W}_{\rm Sk}(\tau)$] displays the following correlation with the scale-by-scale energy budget in Fourier space, where we can identify the k dependence of the energy contributions from the terms with coefficients α, Γ_0, and $T^a(k)$ from Eqs. (A1) and (A2), which we show in Fig. 6: The contribution to the energy budget (A1) from the active term, $-2\alpha\mathcal{E}(k)$, is significantly greater than $T^a(k)$, for values of $\alpha < -2$. For values of $\alpha > 2$, where $\mathcal{P}_{\rm Sk} > 0$, the other active term, $-2\Gamma_0 k^2\mathcal{E}(k)$, dominates over $T^a(k)$.

[1] S. Ramaswamy, The mechanics and statistics of active matter, Annu. Rev. Condens. Matter Phys. **1**, 323 (2010).
[2] E. Fodor, C. Nardini, M. E. Cates, J. Tailleur, P. Visco, and F. van Wijland, How Far from Equilibrium Is Active Matter?, Phys. Rev. Lett. **117**, 038103 (2016).
[3] E. Fodor, R. L. Jack, and M. E. Cates, Irreversibility and biased ensembles in active matter: Insights from stochastic thermodynamics, Annu. Rev. Condens. Matter Phys. **13**, 215 (2022).
[4] L. P. Dadhichi, A. Maitra, and S. Ramaswamy, Origins and diagnostics of the nonequilibrium character of active systems, J. Stat. Mech.: Theory Exp. (2018) 123201.
[5] A. Sokolov, I. S. Aranson, J. O. Kessler, and R. E. Goldstein, Concentration Dependence of the Collective Dynamics of Swimming Bacteria, Phys. Rev. Lett. **98**, 158102 (2007).
[6] A. Sokolov and I. S. Aranson, Physical Properties of Collective Motion in Suspensions of Bacteria, Phys. Rev. Lett. **109**, 248109 (2012).
[7] H. H. Wensink, J. Dunkel, S. Heidenreich, K. Drescher, R. E. Goldstein, H. Löwen, and J. M. Yeomans, Meso-scale turbulence in living fluids, Proc. Natl. Acad. Sci. USA **109**, 14308 (2012).
[8] R. Alert, J. Casademunt, and J.-F. Joanny, Active turbulence, Annu. Rev. Condens. Matter Phys. **13**, 143 (2022).
[9] U. Frisch, *Turbulence: The Legacy of A. N. Kolmogorov* (Cambridge University Press, Cambridge, 1995).
[10] H. Rose and P. Sulem, Fully developed turbulence and statistical mechanics, J. Phys. (Paris) **39**, 441 (1978).
[11] H. Xu, A. Pumir, G. Falkovich, E. Bodenschatz, M. Shats, H. Xia, N. Francois, and G. Boffetta, Flight–crash events in turbulence, Proc. Natl. Acad. Sci. USA **111**, 7558 (2014).
[12] J. Jucha, H. Xu, A. Pumir, and E. Bodenschatz, Time-reversal-symmetry Breaking in Turbulence, Phys. Rev. Lett. **113**, 054501 (2014).
[13] M. K. Verma, Asymmetric energy transfers in driven nonequilibrium systems and arrow of time, Eur. Phys. J. B **92**, 190 (2019).
[14] M. Chertkov, A. Pumir, and B. I. Shraiman, Lagrangian tetrad dynamics and the phenomenology of turbulence, Phys. Fluids **11**, 2394 (1999).
[15] H. Xu, A. Pumir, and E. Bodenschatz, Lagrangian view of time irreversibility of fluid turbulence, Sci. China Phys. Mech. Astron. **59**, 614702 (2016).
[16] A. Pumir, H. Xu, E. Bodenschatz, and R. Grauer, Single-Particle Motion and Vortex Stretching in Three-Dimensional Turbulent Flows, Phys. Rev. Lett. **116**, 124502 (2016).
[17] G. Falkovich and A. Frishman, Single Flow Snapshot Reveals the Future and the Past of Pairs of Particles in Turbulence, Phys. Rev. Lett. **110**, 214502 (2013).
[18] A. Bhatnagar, A. Gupta, D. Mitra, and R. Pandit, Heavy inertial particles in turbulent flows gain energy slowly but lose it rapidly, Phys. Rev. E **97**, 033102 (2018).
[19] K. Pietrzyk, J. A. Horwitz, F. M. Najjar, and R. W. Minich, On analysis and stochastic modeling of the particle kinetic energy equation in particle-laden isotropic turbulent flows, Phys. Fluids **34**, 013316 (2022).
[20] J. R. Picardo, A. Bhatnagar, and S. S. Ray, Lagrangian irreversibility and Eulerian dissipation in fully developed turbulence, Phys. Rev. Fluids **5**, 042601(R) (2020).
[21] S. S. Ray, Non-intermittent turbulence: Lagrangian chaos and irreversibility, Phys. Rev. Fluids **3**, 072601(R) (2018).
[22] P. Švančara and M. La Mantia, Flight-crash events in superfluid turbulence, J. Fluid Mech. **876**, R2 (2019).
[23] A. K. Verma, S. Shukla, V. Shukla, A. Bhatnagar, and R. Pandit, Heavy inertial particles in superfluid turbulence: Coflow and counterflow, Phys. Fluids **35**, 015153 (2023).
[24] J. Dunkel, S. Heidenreich, M. Bär, and R. E. Goldstein, Minimal continuum theories of structure formation in dense active fluids, New J. Phys. **15**, 045016 (2013).
[25] J. Dunkel, S. Heidenreich, K. Drescher, H. H. Wensink, M. Bär, and R. E. Goldstein, Fluid Dynamics of Bacterial Turbulence, Phys. Rev. Lett. **110**, 228102 (2013).
[26] J. Słomka and J. Dunkel, Generalized Navier-Stokes equations for active suspensions, Eur. Phys. J.: Spec. Top. **224**, 1349 (2015).

[27] M. Linkmann, G. Boffetta, M. C. Marchetti, and B. Eckhardt, Phase Transition to Large Scale Coherent Structures in Two-Dimensional Active Matter Turbulence, Phys. Rev. Lett. **122**, 214503 (2019).
[28] M. Linkmann, M. C. Marchetti, G. Boffetta, and B. Eckhardt, Condensate formation and multiscale dynamics in two-dimensional active suspensions, Phys. Rev. E **101**, 022609 (2020).
[29] J. Słomka and J. Dunkel, Spontaneous mirror-symmetry breaking induces inverse energy cascade in 3D active fluids, Proc. Natl. Acad. Sci. USA **114**, 2119 (2017).
[30] V. Bratanov, F. Jenko, and E. Frey, New class of turbulence in active fluids, Proc. Natl. Acad. Sci. USA **112**, 15048 (2015).
[31] A. U. Oza, S. Heidenreich, and J. Dunkel, Generalized Swift-Hohenberg models for dense active suspensions, Eur. Phys. J. E **39**, 97 (2016).
[32] N. Rana and P. Perlekar, Coarsening in the two-dimensional incompressible Toner-Tu equation: Signatures of turbulence, Phys. Rev. E **102**, 032617 (2020).
[33] S. P. Thampi, R. Golestanian, and J. M. Yeomans, Velocity Correlations in an Active Nematic, Phys. Rev. Lett. **111**, 118101 (2013).
[34] S. Thampi and J. Yeomans, Active turbulence in active nematics, Eur. Phys. J.: Spec. Top. **225**, 651 (2016).
[35] L. Puggioni, G. Boffetta, and S. Musacchio, Giant vortex dynamics in confined bacterial turbulence, Phys. Rev. E **106**, 055103 (2022).
[36] M. Bär, R. Großmann, S. Heidenreich, and F. Peruani, Self-propelled rods: Insights and perspectives for active matter, Annu. Rev. Condens. Matter Phys. **11**, 441 (2020).
[37] Equation (3) is not Galilean invariant; it reduces to the Navier-Stokes equation with friction for $\Gamma_0 > 0$, $\alpha > 0$, $\Gamma_2 = 0$, $\lambda_0 = 1$, and $\beta = 0$.
[38] This is similar to energy injection in the Kuramoto-Sivashinsky equation (see, e.g., Refs. [58–60]).
[39] M. James, W. J. T. Bos, and M. Wilczek, Turbulence and turbulent pattern formation in a minimal model for active fluids, Phys. Rev. Fluids **3**, 061101(R) (2018).
[40] P. Perlekar, S. S. Ray, D. Mitra, and R. Pandit, Persistence Problem in Two-Dimensional Fluid Turbulence, Phys. Rev. Lett. **106**, 054501 (2011).
[41] C. Canuto, M. Y. Hussaini, A. Quarteroni, and T. A. Zhang, *Spectral Methods in Fluid Dynamics* (Springer, New York, 2012).
[42] S. M. Cox and P. C. Matthews, Exponential time differencing for stiff systems, J. Comput. Phys. **176**, 430 (2002).
[43] C. P. Sanjay and A. Joy, Friction scaling laws for transport in active turbulence, Phys. Rev. Fluids **5**, 024302 (2020).
[44] M. James and M. Wilczek, Vortex dynamics and Lagrangian statistics in a model for active turbulence, Eur. Phys. J. E **41**, 21 (2018).
[45] S. Mukherjee, R. K. Singh, M. James, and S. S. Ray, Anomalous Diffusion and Lévy Walks Distinguish Active from Inertial Turbulence, Phys. Rev. Lett. **127**, 118001 (2021).
[46] R. K. Singh, S. Mukherjee, and S. S. Ray, Lagrangian manifestation of anomalies in active turbulence, Phys. Rev. Fluids **7**, 033101 (2022).
[47] For conventional 2D fluid turbulence, Refs. [11,61] discuss, for both DNSs and experiments, the effects of different types of forcing on $\mathcal{P}_{\rm Sk}$. They report $\mathcal{P}_{\rm Sk} < 0$ in DNSs with white-noise forcing; by contrast, in Faraday-wave experiments, they observe $\mathcal{P}_{\rm Sk} > 0$, which they attribute to the temporal coherence of Faraday waves. In the latter case they employ a filtering procedure that again yields $\mathcal{P}_{\rm Sk} < 0$. In the Supplemental Material we investigate the effects of a similar filtering procedure for 2D bacterial turbulence in Eq. (3).
[48] See Supplemental Material at http://link.aps.org/supplemental/10.1103/PhysRevFluids.8.023102 for details.
[49] This widening could be a signature of intermittency effects, which we examine elsewhere [62,63].
[50] A. Okubo, Horizontal dispersion of floatable particles in the vicinity of velocity singularities such as convergences, in *Deep Sea Research and Oceanographic Abstracts* (Elsevier, New York, 1970), Vol. 17, pp. 445–454.
[51] J. Weiss, The dynamics of enstrophy transfer in two-dimensional hydrodynamics, Phys. D (Amsterdam) **48**, 273 (1991).

[52] L. Giomi, Geometry and Topology of Turbulence in Active Nematics, Phys. Rev. X **5**, 031003 (2015).
[53] Similar PDFs have been obtained in Ref. [46], but the power-law form has not been noted.
[54] R. Alert, J.-F. Joanny, and J. Casademunt, Universal scaling of active nematic turbulence, Nat. Phys. **16**, 682 (2020).
[55] L. H. Cisneros, J. O. Kessler, S. Ganguly, and R. E. Goldstein, Dynamics of swimming bacteria: Transition to directional order at high concentration, Phys. Rev. E **83**, 061907 (2011).
[56] R. Chatterjee, N. Rana, R. A. Simha, P. Perlekar, and S. Ramaswamy, Inertia Drives a Flocking Phase Transition in Viscous Active Fluids, Phys. Rev. X **11**, 031063 (2021).
[57] M. J. Bowick, N. Fakhri, M. C. Marchetti, and S. Ramaswamy, Symmetry, Thermodynamics, and Topology in Active Matter, Phys. Rev. X **12**, 010501 (2022).
[58] Y. Kuramoto and T. Tsuzuki, Persistent propagation of concentration waves in dissipative media far from thermal equilibrium, Prog. Theor. Phys. **55**, 356 (1976).
[59] G. I. Sivashinsky, Nonlinear analysis of hydrodynamic instability in laminar flames—I. Derivation of basic equations, Acta Astronaut. **4**, 1177 (1977).
[60] D. Roy and R. Pandit, One-dimensional Kardar-Parisi-Zhang and Kuramoto-Sivashinsky universality class: Limit distributions, Phys. Rev. E **101**, 030103(R) (2020).
[61] A. Pumir, H. Xu, G. Boffetta, G. Falkovich, and E. Bodenschatz, Redistribution of Kinetic Energy in Turbulent Flows, Phys. Rev. X **4**, 041006 (2014).
[62] K. Kolluru, A. Gupta, A. Verma, and R. Pandit (unpublished).
[63] M. Cencini, L. Biferale, G. Boffetta, and M. De Pietro, Time irreversibility and multifractality of power along single particle trajectories in turbulence, Phys. Rev. Fluids **2**, 104604 (2017).